A Wireless Miniature Injectable Device with Memory-Assisted Backscatter for Multimodal Animal Physiological Monitoring

Yiming Han[1], *Graduate Student Member*, *IEEE*, Raymond G Stephany[1], *Member*, *IEEE*, Linran Zhao[1], *Graduate Student Member*, *IEEE*, Parvez Ahmmed[2], *Member, IEEE*, Alper Bozkurt[2], *Senior Member, IEEE*, Yaoyao Jia[1], *Member*, *IEEE*

***Abstract*— This paper introduces a wirelessly powered multimodal animal physiological monitoring application-specific integrated circuit (ASIC). Fabricated in the 180 nm process, the ASIC can be integrated into an injectable device to monitor subcutaneous body temperature, electrocardiography (ECG), and photoplethysmography (PPG). To minimize the device size, the ASIC employs a miniature receiver (Rx) coil for wireless power receiving and data communication through a single inductive link operating at 13.56 MHz. We propose a folded L-shape Rx coil with improved coupling to the transmitter (Tx) coil, even in the presence of misalignment, and enhanced quality factor. The ASIC functions alternatively between recording and sleeping modes, consuming 2.55 µW on average. For PPG measurements, a reflection-type PPG sensor illuminates an LED with tunable current pulses. A current-input analog frontend (AFE) amplifies the current of a photodiode (PD) with 30.8 pA_{RMS} current input-referred noise (IRN). The ECG AFE captures ECG signals with a configurable gain of 45-80 dB. The temperature AFE achieves 0.02℃ inaccuracy within a sensing range between 27-47℃. The AFE outputs are sequentially digitized by a 10-bit successive approximation register (SAR) analog-to-digital converter (ADC) with an effective number of bits (ENOB) of 8.79. To improve the reliability of data transmission, we propose a memory-assisted backscatter scheme that stores ADC data in an off-chip memory and transmits it when the coupling condition is stable. This scheme achieves a package loss rate (PLR) lower than 0.2 % while allowing 24-hour data storage. The device's functionality has been evaluated by in vivo experiments.**

Index Terms—***injectable device, multimodal sensing, backscatter transmitter, wireless power, memory controller***

This work was supported by the United States National Science Foundation (NSF) under Grant ECCS-2151788, Grant ECCS-2239915, Grant IIS-2319060, Grant IIS-2037328, Grant EF-2319389, Grant CCSS-1554367, and Grant ECC-1160483 (NSF Nanosystems Engineering Research Center for Advanced Self-Powered Systems of Integrated Sensors and Technologies (ASSIST)).

Y. Han, R. Stephany, L. Zhao, and Y. Jia are with the Chandra Family Department of Electrical and Computer Engineering, The University of Texas at Austin, Austin, TX 78712, USA (email: ymhan@utexas.edu, ray.stephany@utexas.edu, lrzhao@utexas.edu, and yjia@austin.utexas.edu).

Parvez Ahmmed and Alper Bozkurt are with the Department of Electrical and Computer Engineering, North Carolina State University, Raleigh, NC 27695, USA (email: pahmmed@ncsu.edu and aybozkur@ncsu.edu).

I. Introduction

Wearable technologies, widely employed in human health monitoring, facilitate long-term and continuous data collection in various form factors, such as chest patches, smartwatches and smart glasses [1-6]. However, wearable devices face several challenges when applied to animals, as illustrated in Fig. 1. Animals typically have thick skin, fur, or scales, resulting in inadequate attachment between the wearable device and the animals' tissue. This weak attachment can significantly degrade the recorded physiological signals, resulting in a low signal-to-noise ratio (SNR) [7-12]. Moreover, the weak attachment makes wearable devices susceptible to motion artifacts from freely moving animals, causing strong interference and potentially saturating the analog frontend (AFE) [13-20].

To overcome these challenges, researchers have proposed implantable devices that show great potential to accurately monitor animal physiological signals [21-25]. These implantable devices, placed subcutaneously, ensure strong tissue coupling, effectively eliminating signal degradation and enhancing SNR. Additionally, the firm anchoring of implantable devices within the tissue minimizes interference from motion artifacts [26-30].

Wireless technologies also benefit implantable devices. Implementing wireless power transfer (WPT) and data communication eliminates bulky batteries and wire connections, effectively reducing interruptions for battery replacement and facilitating device miniaturization. The miniature device results in less invasiveness and a smaller burden on animals. Furthermore, wireless operation facilitates remote physiological monitoring and data analysis, reducing interferences and stress on animal subjects. However, the miniature size of the device limits the receiver (Rx) coil size, which decreases the quality (Q) factor and compromises the mutual inductance coefficient with the transmitter (Tx) coil. These limitations significantly reduce the power transfer efficiency (PTE), resulting in a limited power budget.

To address this limitation, recently reported implantable devices [21-23, 25, 31] have employed area and energy-efficient designs, achieving miniature devices and low

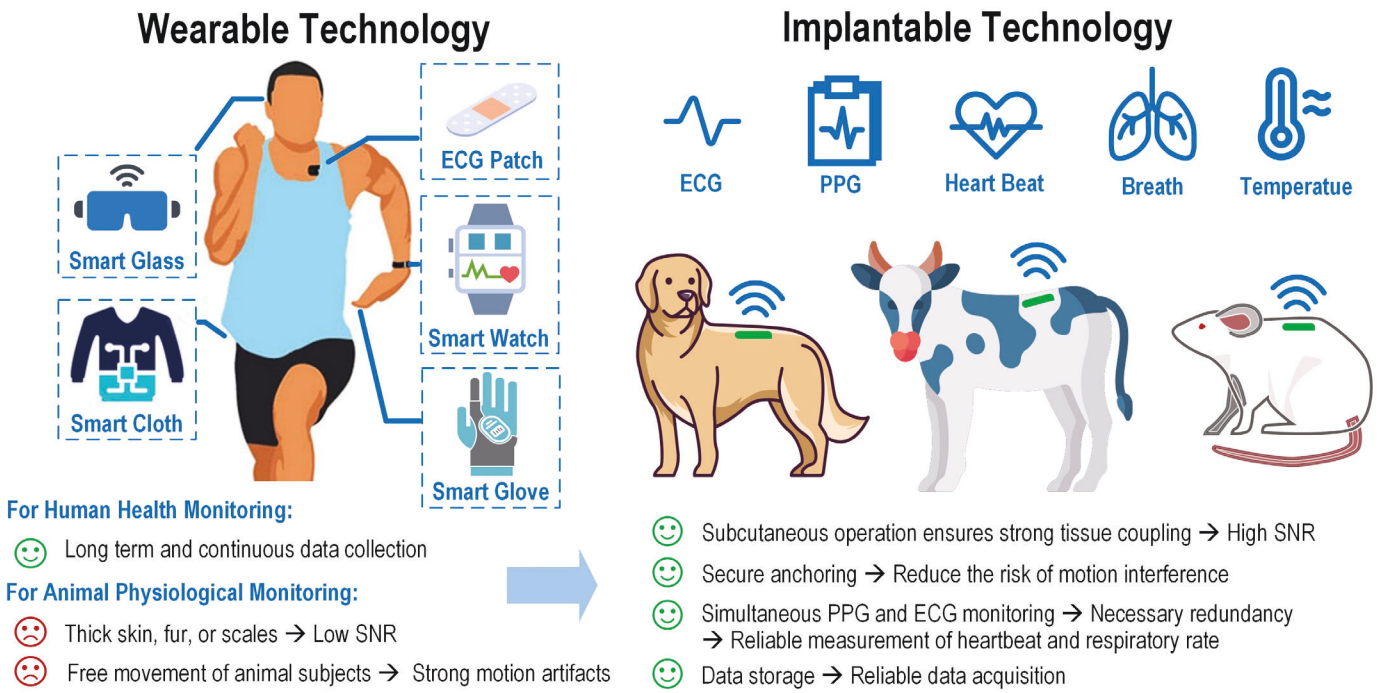

Fig. 1. Comparison of wearable and implantable technologies for animal physiological monitoring.

power consumption of less than 300 μW. However, these designs only provide single photoplethysmography (PPG) sensing or electrical and temperature recording, respectively. The limited sensing modalities cannot offer the necessary redundancy for accurate animal physiological monitoring.

Additionally, low PTE poses challenges for wireless data communication. To ensure sufficient power delivery to the load (PDL) with a miniature coil size, the inductive link requires higher input power, which increases interference within data communication and reduces its reliability. [24] proposed a wireless injectable application-specific integrated circuit (ASIC) with an on-chip coil, achieving both WPT and bidirectional wireless data communication on a miniature ASIC. However, the miniature on-chip coil requires a high output power of 28 dBm on the Tx antenna to ensure adequate PDL, introducing significant interference to wireless data communication.

Furthermore, the free movement of the animals, which causes coil misalignment, also challenges the reliability of wireless data communication. In our previous work [32], we proposed a wireless multimodal injectable device capable of continuous wireless data transmission. However, the reliability of wireless data transmission can be compromised when the coupling condition is weak due to the free movement of the animals.

To address challenges in existing implantable devices and ASICs, this paper presents a wireless multimodal physiological monitoring ASIC that can be encapsulated into an injectable implant to measure subcutaneous body temperature, PPG, and electrocardiography (ECG) in animals. Significant efforts are made to achieve a miniature device size to minimize invasiveness. First, the injectable device is wirelessly powered by an inductive link operating at 13.56 MHz, which also serves as the data link for command reception and data transmission. This configuration utilizes an Rx coil shared for both data communication and WPT, eliminating the need for additional data coils/antennas. Second, the Rx coil employs a folded L-shape design, which improves the Q-factor and mutual inductance coefficient with the Tx coil for higher PTE under the miniature device size. Third, the proposed ASIC functions alternatively between regular recording and power-saving sleep modes to reduce average power consumption. Moreover, we implement a passive backscatter Tx, eliminating the conventional power-consuming active radio. Thanks to these low-power designs, the device can receive sufficient power without enlarging the coil and device. For reliable data transmission despite animal movements, we propose a memory-assisted technique employed in the Tx that stores recorded data in an off-chip memory and transmits it when the inductive link stabilizes, enhancing transmission reliability.

In this paper, Section II offers an overview of the proposed wireless multimodal physiological monitoring ASIC and introduces detailed circuit implementation of each block. Section III presents measured ASIC characterizations and compares them with state-of-the-art designs. Section IV introduces wireless power and data communication verification as well as in-vivo experiments evaluating device functionality. Section IV discusses future works for further employing the proposed device on freely moving animals. Finally, Section V concludes the paper.

II. Circuit Implementation

Fig. 2 illustrates the proposed wirelessly powered miniature injectable device. The device integrates the proposed wireless multimodal physiological monitoring ASIC wire-bounded on its top, while a PPG sensor including a photodiode (PD) and a green light-emitting diode (LED), an ECG electrode, a memory

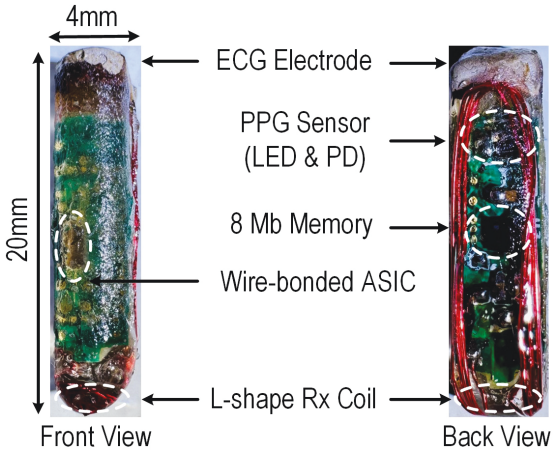

Fig. 2. Photo of the assembled wirelessly powered miniature injectable device.

chip, and the proposed L-shape Rx coil are soldered at its bottom. The injectable device is encapsulated in a cylindrical form factor measuring 2 cm in length and 4 mm in diameter using medical-grade epoxy glue, which is highly biocompatible, ensuring safety for long-term implantation [33]. Because of our efforts in device miniaturization, the device supports multiple sensing modalities and data storage for reliable data transmission while maintaining a comparable device size to other recently reported implantable devices [21-25]. Furthermore, by removing unnecessary testing pads on the ASIC to simplify its wire bonding, the device size can be further reduced to 1 cm in length and 2 mm in diameter in our future works. The ECG electrode, constructed with conductive epoxy, is directly deposited on the device's tip. This placement facilitates secure attachment both to the ECG input pads on the device's side and to tissue, ensuring a robust collection of the ECG signal. The L-shape Rx coil, featuring 2.4 cm length, 4 mm width, and 3 turns, enhances its surface area, which optimizes the Q-factor and improves PTE. The enhanced surface area also promotes robust coupling with the Tx coil, mitigating coil misalignment issues. Furthermore, the L-shaped design allows the coil to wrap around the device, minimizing its impact on the overall device size.

Fig. 3 depicts the block diagram of the proposed wireless multimodal physiological monitoring ASIC, which is wirelessly powered by a 3-coil inductive link ($L_1 \rightarrow L_2 \rightarrow L_3$) operating at 13.56 MHz. L_1, driven by a power amplifier (PA), serves as the Tx coil, while L_2 is the Tx resonator consisting of an LC tank resonating at 13.56 MHz. The coupling between L_1 and L_2 is optimized outside of the animal body. To improve power stability, a 100 µF supercapacitor, C_S, is added to the output of the voltage doubler, which rectifies and stores the received power from the L-shape Rx coil (L_3) to C_S. This supercapacitor serves as a temporary power source when the inductive link is unstable due to animal movement. A low dropout regulator (LDO) then regulates V_{DBR} to a 1.8 V supply voltage, V_{DD}, for the ASIC and an 8 Mb memory chip. Meanwhile, a microcontroller unit (MCU) modulates the 13.56 MHz carrier using OOK modulation by activating and deactivating the PA to transmit the user command to the ASIC. The L_3 receives the modulated carrier V_{COIL}, which is then demodulated in the forward data telemetry to recover the user command to configure the AFEs. The AFEs capture ECG, PPG, and temperature. The signal digitizer periodically digitizes the AFE outputs, resulting in 13-bit data packages, including 10-bit data and a 3-bit channel identifier (ID) [32]. The data packages can be transmitted wirelessly to an external data Rx, i.e., software-defined radio (SDR, BladeRF x40) through a 4-coil inductive link ($L_3 \rightarrow L_2 \rightarrow L_1 \rightarrow L_4$) using two user-defined routes. It can be continuously and wirelessly transmitted to the SDR Rx through the backscatter Tx. Additionally, it can be routed to the memory controller for data storage in an 8 Mb off-chip serial flash memory (W25Q80EW) via the serial peripheral interface (SPI). Once the data transmission is needed or the stored data exceeds the maximum storage of the memory chip, stored data is forwarded to the backscatter Tx and transmitted wirelessly to the SDR Rx. and transmitted wirelessly to the SDR Rx.

The ECG AFE adopts a two-stage amplification configuration consisting of a low-noise amplifier (LNA) and a variable-gain amplifier (VGA) to amplify the input signal, ECG_{IN}, captured by the ECG electrode [34], as shown in Fig. 4. The LNA employs an AC-coupled input to block the DC voltage from the tissue interface and ECG electrode. The LNA functions as a bandpass filter, whose low-cutoff frequency is set by $1/2\pi C_2 R_1$, the mid-band gain is determined by C_2/C_1, and

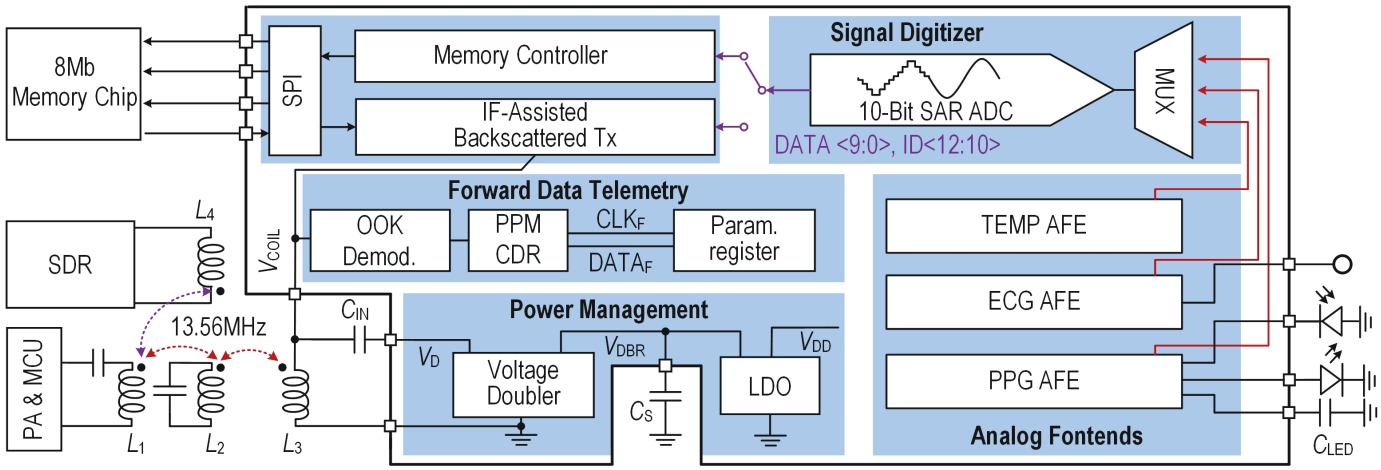

Fig.3 Block diagram of the wireless multimodal physiological monitoring ASIC.

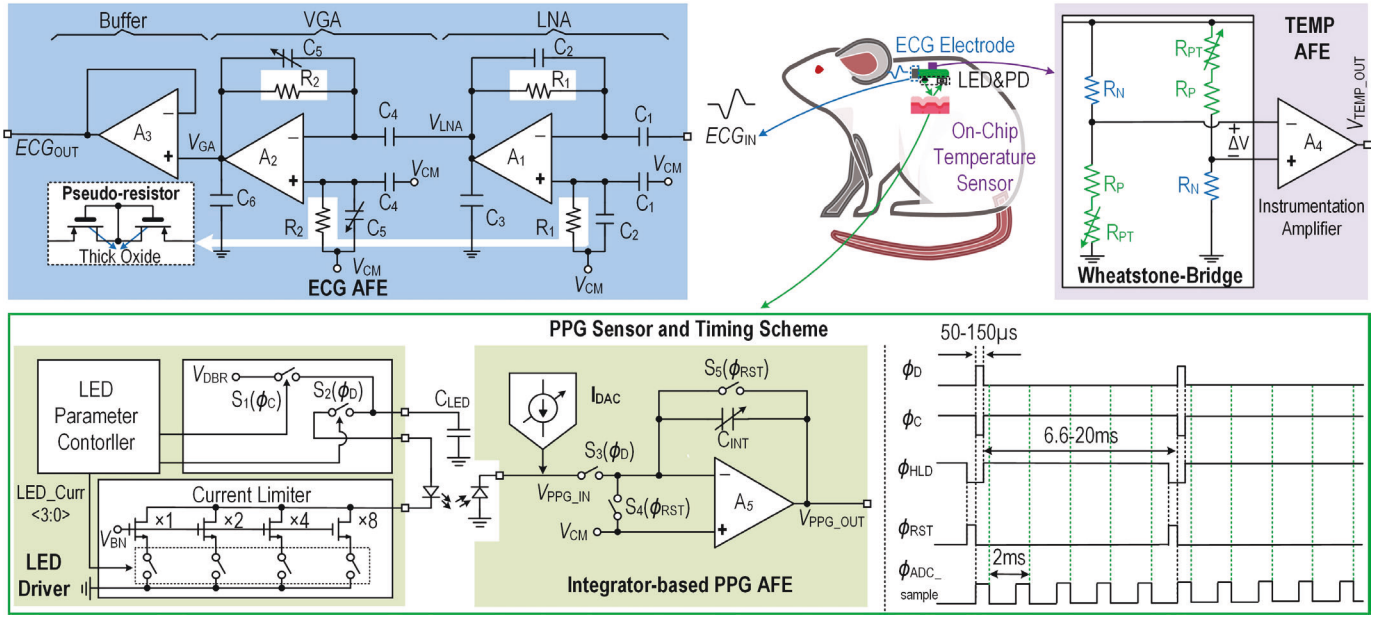

Fig. 4. Schematic of AFEs for ECG recording, body temperature monitoring, and PPG measurement.

the input impedance is set by $1/2\pi fC_1$. Specifically, R_1, a pseudo resistor consisting of thick oxide transistors, minimizes current leakage while providing resistance at the giga-ohm level in a compact silicon area, resulting in a low-cutoff frequency below 1 Hz to avoid filtering out the low-frequency ECG signals. The VGA amplifies the LNA output with a variable voltage gain setting by C_5/C_4, where C_5 is a digitally controlled capacitor array. An analog buffer offers anti-aliasing low-pass filtering and sufficient driving capability for the subsequent successive approximation register (SAR) analog-to-digital converter (ADC). In body temperature AFE, a Wheatstone bridge (WhB) incorporates two types of resistors, R_N and R_P/R_{PT}, with opposing temperature coefficients (TC). Specifically, R_N, an n-type poly resistor, exhibits negative TC, while R_P, a p-type poly resistor, has positive TC. This configuration converts the temperature into a DC voltage, which is further amplified by a current feedback instrumental amplifier (CFIA). To accommodate the typical animal body temperature range (27-47℃), the sensing range of the temperature AFE is configured accordingly. Given that the sensitivity of the WhB is 20 mV/℃, we design the voltage gain of the CFIA to 30 dB, resulting in a resolution of 0.03℃, suitable for precise animal health monitoring [35]. To alleviate inaccuracies due to process variations, we adopt two 3-bit binary weighted resistor arrays, R_{PT}, for process variation trimming.

For PPG measurement, we employ a reflection-type PPG sensor illustrated in Fig. 4. A switch-capacitor (SC)-based LED driver charges an off-chip storage capacitor, C_{LED}, to V_{DBR} by activating switch S_1 during a long charging phase (Φ_C) of 6.6–20 ms. In the subsequent discharging phase (Φ_D), S_1 is switched off while S_2 is activated to discharge C_{LED}, illuminating the green LED with a programmable frequency (50-150 Hz) and pulse width (50-150 μs). This approach allows the C_{LED} to accumulate sufficient charge during Φ_C, ensuring it can supply the 15 mA LED driving current in the presence of fluctuations in the inductive link. A current limiter adjusts the discharging current from 1 to 15 mA, controlling LED brightness. The light of the LED is reflected by the blood vessel and captured by the PD, producing a current signal. Concurrently, the S_3 is activated, directing the current-input integrator-based PPG AFE to integrate and amplify the current signal with an adjustable transimpedance ranging from 2.5 to 40 MΩ. A current digital-to-analog converter (IDAC) injects a programmable current from 0.25 to 4 μA to cancel the baseline current of the PD, avoiding saturation of the PPG AFE. The integrated voltage is stored on a feedback capacitor, C_{INT}, for subsequent ADC sampling during the holding phase (Φ_{HLD}). In the reset phase (Φ_{RST}), the S_4 and S_5 are turned on, controlling the PPG AFE to function as an analog buffer to reset the voltage across the C_{INT} before the next Φ_D. Fig. 5b details the timing scheme of the PPG. This timing configuration eliminates the need for synchronizing the ADC sampling clock with LED control timing, allowing for shared ADC usage among other AFEs.

Fig. 5 illustrates the comparison of the proposed two user-defined routes for data storage and transmission. Directly transmitting data packages to the backscatter Tx enables continuous real-time monitoring and data processing. However, this method can suffer from high data loss due to potential power variations and coil misalignments resulting from the free movement of animals. To address this limitation, we propose a more reliable memory-assisted scheme, where an off-chip 8 Mb memory chip functions as a data buffer. Specifically, the data packages from the signal digitizer are first written into the memory chip during the writing mode and then forwarded to the backscatter Tx for data communication when the inductive link stabilizes. In the writing mode, a memory controller stores data packages from the signal digitizer in an on-chip 16-bit 8-entry first-in-first-out (FIFO) buffer at the data rate of 15 kb/s. These stored data packages are then sent to the memory chip through an SPI interface at a higher data rate of 50 kb/s. This configuration ensures that the output bandwidth of the FIFO

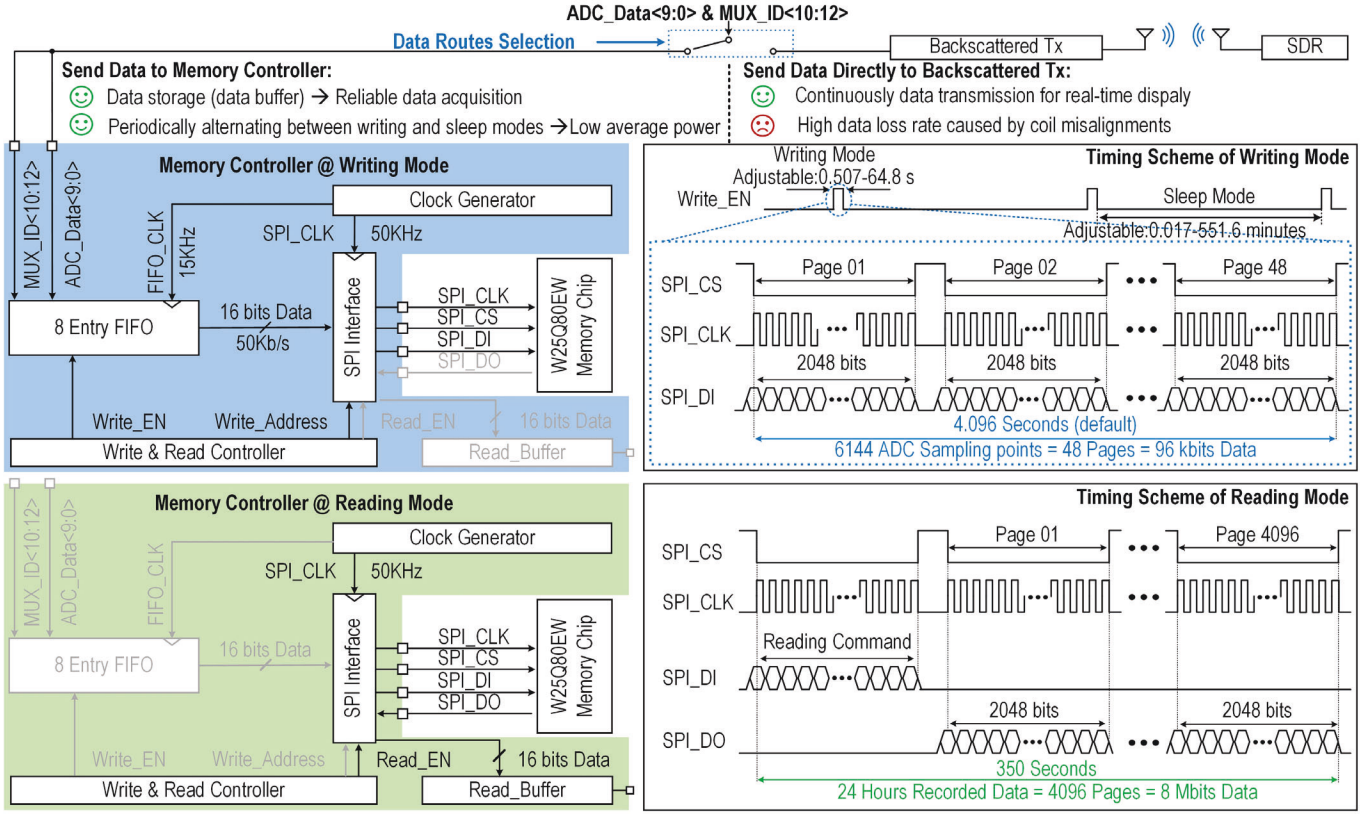

Fig. 5. Two user-defined routes for data storage and transmission and structure of the memory controller, as well as the timing scheme in writing and reading mode.

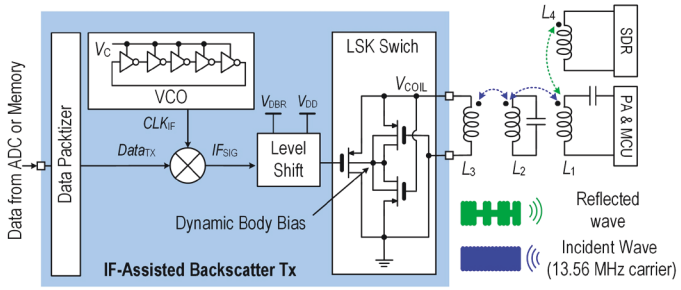

Fig. 6. Schematic of the IF-assisted backscatter Tx.

exceeds its input bandwidth, preventing data overwriting. Furthermore, the memory controller extends each data package to 16 bits, allowing each page of the memory chip to store 128 data packages. The ASIC alternates between the writing mode, with a user-defined duration from 0.507 to 64.8 s, and a power-saving sleep mode, where only the forward data telemetry is active, with a user-defined duration from 0.017 to 551.6 minutes. This periodic operation not only significantly reduces the average power consumption of the ASIC but also enables 24-hour data storage under the default setup: a writing mode duration of 4.096 s stores 4166 data packages in 48 pages, followed by a sleep mode duration of 1034.24 s. When data transmission is needed, the memory controller reads the stored data packages into a 16-bit data buffer at a data rate of 50 kb/s via an SPI interface before sending them to the backscatter Tx. The reading mode requires 350 seconds to read all 8 Mb of data.

Fig. 6 shows the schematic of the intermediate frequency (IF)-assisted load-shift keying (LSK) backscatter Tx. The data packetizer packetizes the data from the signal digitizer or the memory chip with 8-bit preambles, forming the backscatter data, $Data_{TX}$. The $Data_{TX}$ is then mixed with the IF clock, CLK_{IF}, generated by a voltage-controlled oscillator (VCO), resulting in IF_{SIG}. The IF_{SIG} is subsequently level-shifted to V_{DBR} to control the LSK switch which modulates the load impedance on L_3, altering the reflection coefficient of the inductive link and modulating the carrier amplitude. This scheme requires only a few passive switches, achieving high energy efficiency and simplifying circuit implementations, making it well-suited for our ASIC with limited power and area budgets. Additionally, the IF operation translates the backscatter data to a frequency sideband that is CLK_{IF} away from the carrier frequency. This allows the SDR Rx to effectively filter out the carrier while receiving the backscatter signal through the 4-coil inductive link ($L_3 \rightarrow L_2 \rightarrow L_1 \rightarrow L_4$) for further demodulation and data analysis. This method mitigates the risk of saturation and interference from the high-power carrier, ensuring the SDR Rx can accurately recover backscatter data. Given that the L_3 also receives wireless power, we employ a dynamic body bias, which always connects the bulk of the switch transistor to the highest voltage to avoid latch-up issues under high carrier power.

In Fig. 7, the reflected carrier is received by L_4. Thanks to the IF-assisted scheme, the bandpass filter can effectively filter out the 13.56 MHz carrier, allowing the analog receiver to amplify, down-convert, and filter the backscattered signal in the SDR without the risk of saturation from the high-power carrier. The output signal is then oversampled at a sampling rate of 4 MSps for digitization. The produced 12-bit I & Q data streams are

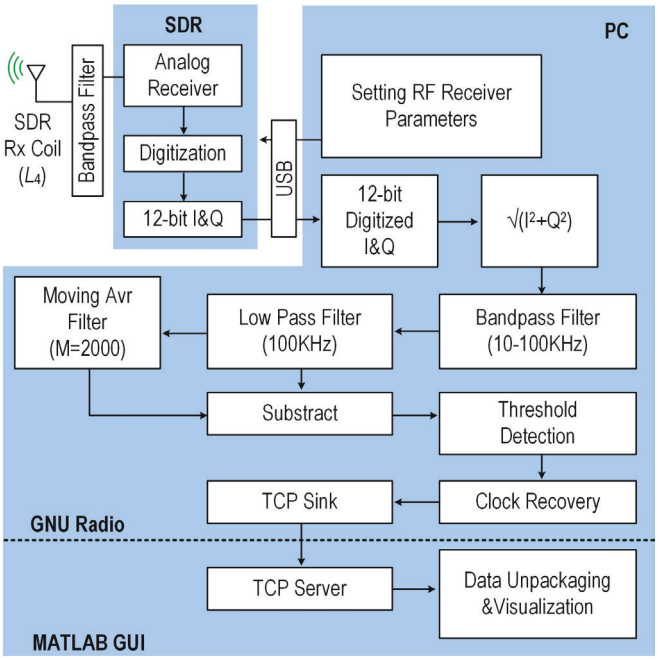

Fig. 7. Simplified algorithm architecture of the SDR Rx.

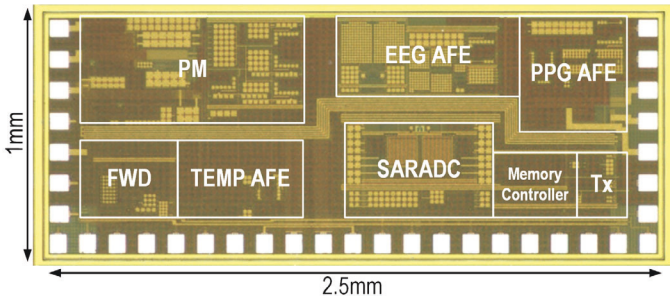

Fig. 8. The micrograph of the wireless multimodal physiological monitoring ASIC.

then sent to GNU Radio running on a PC, where the digital I & Q data are recovered to the analog signals. Additional filtering is applied to remove the analog receiver's DC leakage and high-frequency interference, preparing the signal for the threshold detector, which demodulates the amplitude-modulated signal to recover the backscatter data. Subsequently, a clock recovery algorithm recovers the sampling clock. The recovered data and sampling clock are sent to a MATLAB GUI through a TCP link for data unpackaging and remote monitoring.

III. Measurement Results

Fig. 8 shows the micrograph of the proposed wireless multimodal physiological monitoring ASIC. The ASIC, fabricated in the TSMC 180 nm standard CMOS process, occupies a silicon area of 2.5 × 1 mm^2, including testing pads.

Fig. 9a and Fig. 9b illustrate the measured input-referred noise (IRN) power density spectrum (PSD) and frequency response of the ECG AFE, respectively. The IRN PSD shows a flicker noise corner at approximately 10 Hz and a thermal noise floor of 30 nV/√Hz, resulting in an integrated IRN of 0.99 μV_{RMS} within 0.1-150 Hz. The frequency response of the ECG AFE displays a bandpass characteristic with a low cutoff

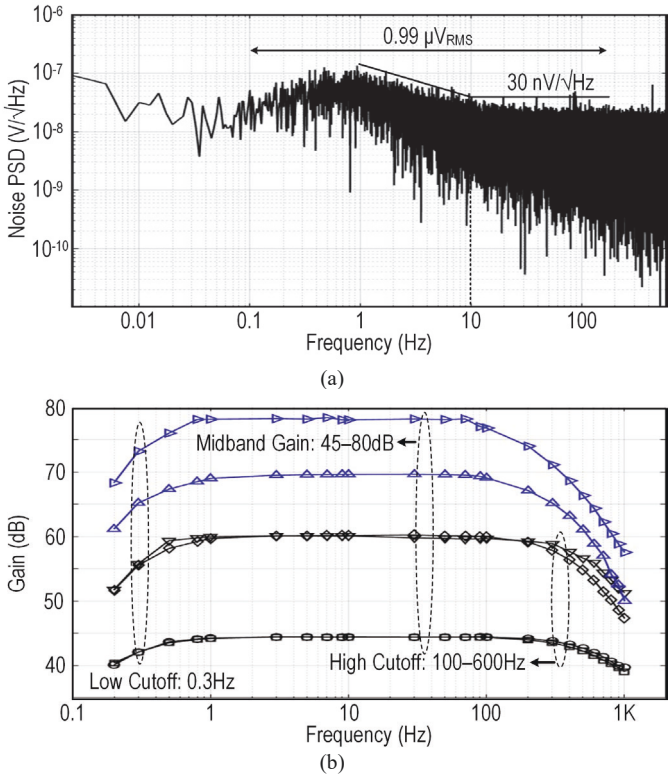

Fig. 9. Measured (a) input-referred PSD and (b) AC response of the ECG AFE.

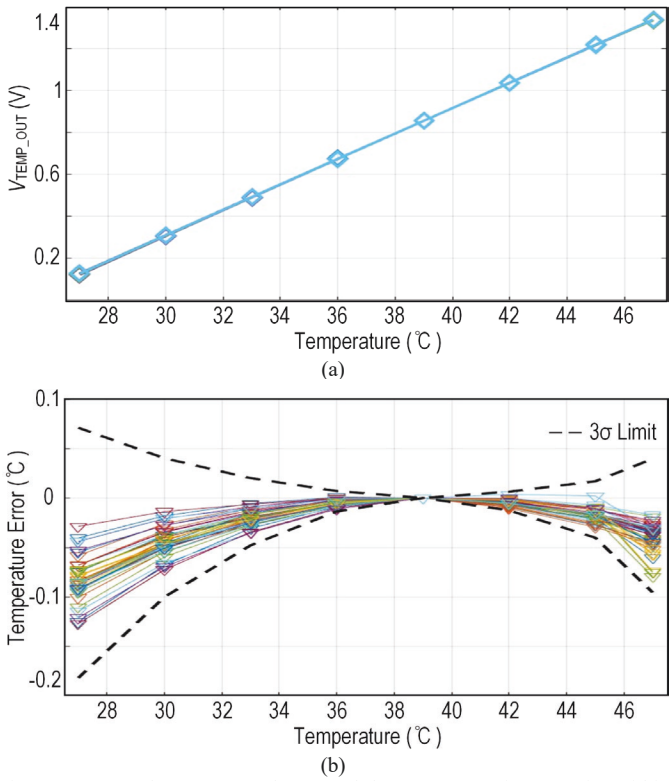

Fig. 10. Measured (a) output voltages and (b) temperature inaccuracies within 27-47℃ of the temperature AFE.

frequency of 0.3 Hz, a programmable midband gain of 45-80 dB, and a tunable high cutoff frequency of 100-600 Hz.

To measure the output voltages and inaccuracy of the body temperature AFE under different temperatures, we first trim the values of R_{PT} in the temperature AFEs on 20 ASICs at 39℃. Subsequently, we vary the temperature from 27 to 47℃ to

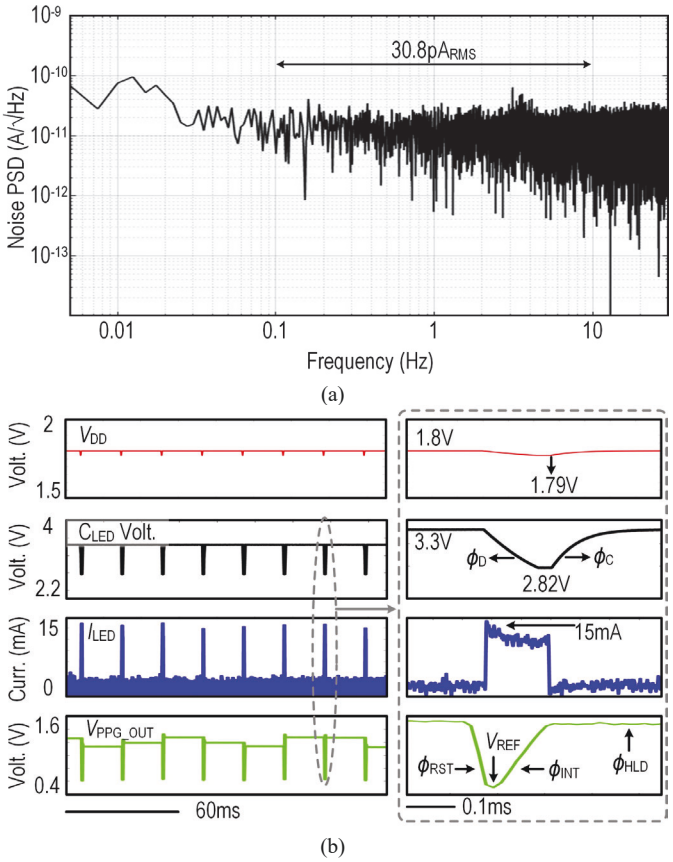

Fig. 11. Measured (a) input-referred noise PSD and (b) transient waveforms of the PPG measurement.

.

measure their output voltages. Calibration is performed based on the output voltage measured at 39℃. The measured output voltages and the temperature inaccuracy after calibration are presented in Fig. 10a and Fig. 10b, respectively. The temperature AFE can sense the temperature between 27 and 47℃ with inaccuracy below 0.2℃.

Fig. 11a presents the measured IRN PSD of the PPG AFE. The PPG AFE reveals an IRN current of 30.8 pA_{RMS} after integrating the IRN PSD within 0.1-10 Hz. Fig. 11b shows the transient waveform of the PPG measurement in the most power-consuming scenarios with the maximum LED current of 15 mA and the largest Φ_D pulse width of 150 µs. The voltage on C_{LED} is charged to V_{DBR} at 3.3 V during Φ_C. In the subsequent resetting phase, Φ_{RST}, the output voltage of the PPG AFE, V_{PPG_OUT}, is reset to a reference voltage of 0.9 V. Immediately after the resetting, the C_{LED} dumps its charge to the LED, illuminating the LED for 150 µs. With C_{LED} has a capacitance of 4.7 µF, the voltage on C_{LED} experiences a drop of 0.48 V during Φ_D. In the meanwhile, the current-input integrator-based PPG AFE integrates the current from the PD, resulting in the V_{PPG_OUT}. To evaluate whether the voltage doubler can adequately power the PPG sensor, we measured the LDO output, V_{DD}, during the PPG measurement. As shown in Fig. 11b, V_{DD} drops by less than 10 mV during Φ_D, confirming that the LDO provides a stable supply voltage during the PPG measurement. Thanks to the IDAC canceling the baseline current of the PD, the V_{PPG_OUT} does not saturate. Although the small remaining baseline current is still integrated and results in

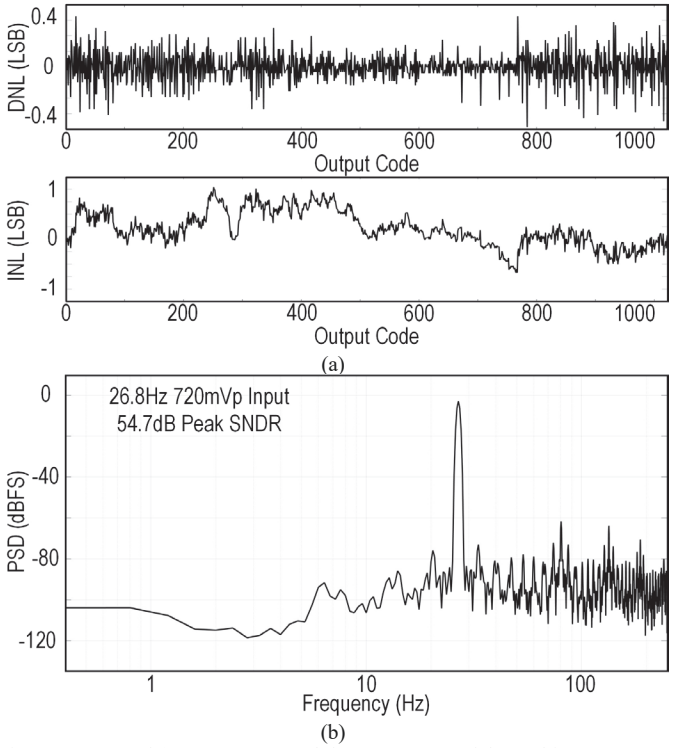

Fig. 12. Measured (a) INL, DNL, and (b) output PSD of the 10-bit SAR ADC.

a DC offset on the V_{PPG_OUT}, we can easily filter it out in the post-data processing. Fig. 12a shows the measured integral nonlinearity (INL) and differential nonlinearity (DNL) of the SAR ADC. We apply a 0-1.8 V linear ramp signal with 50 points per ADC output code to the ADC input. The INL is within (+1.06, -0.46) least significant bit (LSB), while the DNL is within (+0.34, -0.37) LSB. Fig. 12b shows the output PSD of the ADC with a 26.8 Hz, 720 mV_p sinusoidal input. We convert the output ADC data into the analog signal and apply a 30000-point fast-Fourier transformation (FFT) using a Hamming window. The ADC achieves a peak signal-to-noise and distortion ratio (SNDR) of 54.7 dB within the Nyquist bandwidth of 250 Hz, indicating an effective number of bits (ENOB) of 8.79 bits.

To evaluate the IF-assisted backscatter Tx, we tune the on-chip VCO to generate the CLK_{IF} at 1.44 MHz. An external RF generator produces a 13.56 MHz carrier with a power of 10 dBm. A spectrum analyzer receives the reflected backscatter signal. In Fig. 13a, spectrum analysis of the backscattered signal reveals that the backscattered data is translated to the sidebands of 13.56 MHz, i.e., 13.56 MHz±1.44 MHz [36]. Simultaneously, an external SDR Rx receives the backscattered signal for demodulation and data recovery. In the transient measurements shown in Fig. 13b, the consistent data pattern of the backscatter raw signal and the recovered data indicates the backscatter data can be successfully recovered.

Fig. 14 illustrates the power consumption breakdown of the proposed ASIC in three working modes. The writing mode consumes a total power consumption of 515.375 µW. The memory controller consumes the most power, at 70 %, for driving and supplying the memory chip. The PPG AFE accounts for 20 % of the total power, measured under the

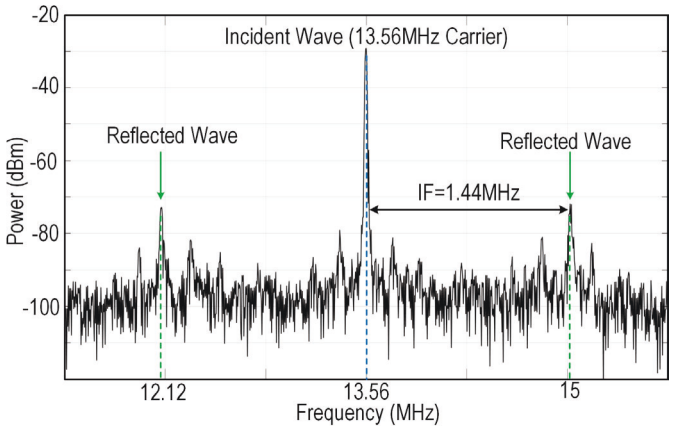

(a)

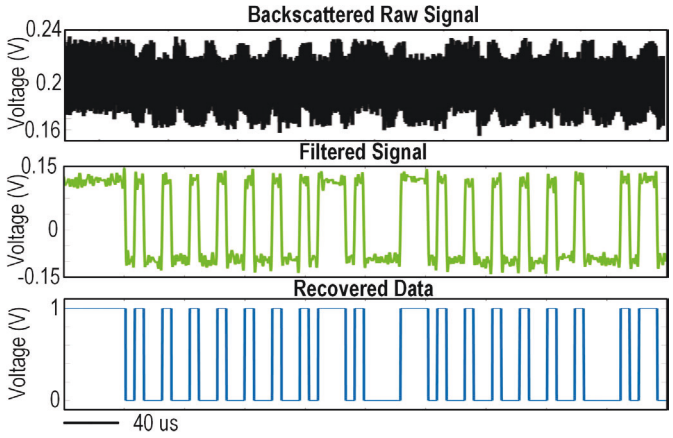

(b)

Fig. 13. Measured (a) output power spectrum and (b) transient waveform of the backscatter Tx.

maximum I_{LED} of 15 mA. The power consumption of the sleep mode is 522 nW, with only the power management and the forward data telemetry on standby for receiving user commands. Therefore, in the default setup with 4.096 s of writing mode and 1034.24 s of sleep mode, the ASIC consumes 2.55 µW on average. Additionally, the reading mode consumes

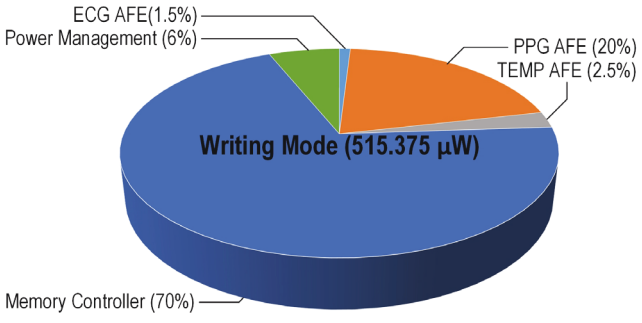

(a)

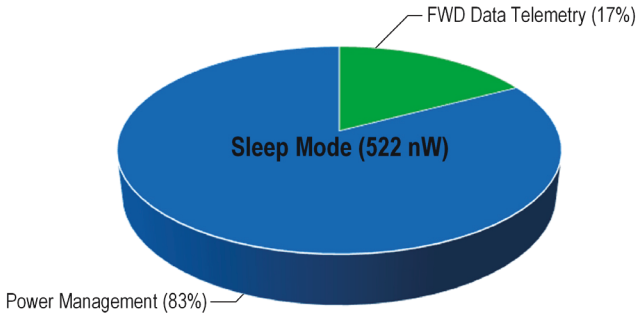

(b)

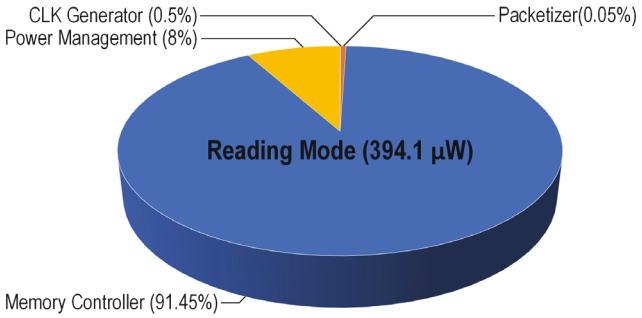

(c)

Fig. 14. Power consumption breakdown of the (a) writing mode, (b) sleep mode, and (c) reading mode.

a total power of 394.1 µW. The memory controller consumes

TABLE I: PERFORMANCE COMPARISON WITH STATE-OF-THE-ART MULTIMODAL PHYSIOLOGICAL MONITORING AISC

	Reference	This Work	[1]	[2]	[23]	[25]	[21]
Injectable Device	Technology	180 nm	180 nm	55 nm	180 nm	130 nm	180 nm
	Chip Area (mm^2)	2.5	0.11	4.5	4.5	6	4.6
	Supply (V)	1.8/3.3	1.8	0.9/1.8/2.8	1.5/2.5	1.2/3.3	-
	Power Source	Inductive Link	Battery	Battery	Capacitive Link	Inductive Link	Magnetoelectric
	Power Consumption	2.55 µW	115 µW[a]	264.6 µW[a]	279.7µW	123 µW[a]	74.8 µW
	Form Factor	Cylindrical Injectable Device	Behind-the-ear Device	Smartwatch	Implantable Device	Implantable Device	Implantable Device
	Sensing Modality	PPG/ECG/TEMP	ExG/PPG/BIOZ GSR/tVNS	ECG/PPG/BIOZ	PPG	Elec. Recording/ TEMP	Elec. Recording
Data Communication	Downlink	OOK-PPM	Bluetooth Low Energy	Wire (I2C/SPI)	-	ASK	Time
	Uplink	IF-LSK Backscatter	Bluetooth Low Energy	Wire (I2C/SPI)	-	LSK Backscatter	PWM Backscatter
	Data Storage	8 Mb Flash Memory	No	16 kb SRAM	No	No	No
	PLR/BER	2×10^{-3} (PLR)	-	-	-	-	8.5×10^{-5} (BER)
ECG/Electrical	IRN (μV_{RMS})	0.99 (0.1-150 Hz)	0.22 (0.5-300 Hz)	0.73 (0.3-150 Hz)	-	7.79 (1-1 kHz)	-
	Power (µW)	5	54	192.6	-	57.6	-
PPG	IRN (pA_{RMS})	30.8 (0.1-10 Hz)	-	100[a] (0.1-20 Hz)	162[a] (0.1-10 Hz)	-	-
	Max I_{LED} (mA)	15	0.11	-	92.3	-	-
	Power (µW)	105.6[c]	59	72[b]	279.7	-	-
TEMP	Range (℃)	27-47	-	-	-	0-50	-
	Power (µW)	12.6	-	-	-	36	-
	Inaccuracy (℃)	±0.2	-	-	-	-	-
	Resolution (℃)	0.03	-	-	-	0.12	-

[a] Estimated [b] Includes the power of ADC; [c] Measured with max I_{LED}.

91.45 % of the total power since the circuit blocks for signal recording are powered down during the data reading and transmission.

Table I compares the proposed wireless multimodal physiological monitoring ASIC with state-of-the-art designs, including implantable and wearable devices. The proposed ASIC incorporates WPT and wireless data communication and provides multiple sensing modalities for ECG, PPG, and body temperature. Wearable devices in Table 1, such as behind-the-ear devices and smartwatches, cannot be securely attached to animal bodies due to thick skin and cannot be firmly anchored on freely moving animals, even though they offer multimodal sensing capabilities. Additionally, since these devices typically rely on battery power, changing the batteries can interrupt experiments, causing discomfort to the animals. Compared to other implantable devices, the proposed ASIC shows several advantages: multiple sensing modalities, ultra-low power, and reliable data transmission. The ultra-low average power is primarily achieved by alternating between recording and power-saving sleep modes. Furthermore, the passive backscatter Tx design eliminates the power-hungry active data Tx, further reducing power consumption. Additionally, the optimized L-shape Rx coil, shared by both power and data links, contributes to a miniature injectable form factor. To facilitate reliable data transmission, we employ a memory-assisted backscatter Tx. The 8 Mb memory chip, which offers 24-hour data storage, functions as a data buffer, improving the reliability of the data transmission despite the free movement of the animals.

IV. Device Verification

A. Wireless Power and Data Transmission Verification

Fig. 15a and Fig. 15b show the setup and schematic of the wireless power and data transmission verification with the proposed injectable device. The PA generated a 13.56 MHz carrier to drive the L_1 for WPT. An MCU (nRF52832, NORDIC® Semiconductor) converted user commands from a PC into OOK data, which then switched the PA on and off to OOK modulate the 13.56 MHz carrier. The injectable device received the power and user commands through the 3-coil inductive link ($L_1 \rightarrow L_2 \rightarrow L_3$) and transmitted the backscattered signal to the SDR Rx via the 4-coil inductive link ($L_3 \rightarrow L_2 \rightarrow L_1 \rightarrow L_4$). SDR demodulated the backscattered signal and sent it to the GUI running on the PC for data unpackaging and real-time monitoring. Fig. 15c presents the detailed configuration of the coils. L_1-L_2 was well-coupled to transmit wireless power and backscattered signal. L_3 is the proposed L-shaped Rx coil, which was optimized to achieve a Q-factor of 59.4 at 13.56 MHz to maximize PTE. The distance between L_2 and L_3 was set at 10 mm to mimic the distance in real experimental conditions when implanting the injectable device in a rat. L_4, connected to SDR, was well coupled with L_1 to efficiently capture the backscattered signal.

To evaluate the package loss rate (PLR) under different wireless power conditions, we first fixed the L_2-L_3 distance at 10 mm and manually adjusted the PA's output power to control

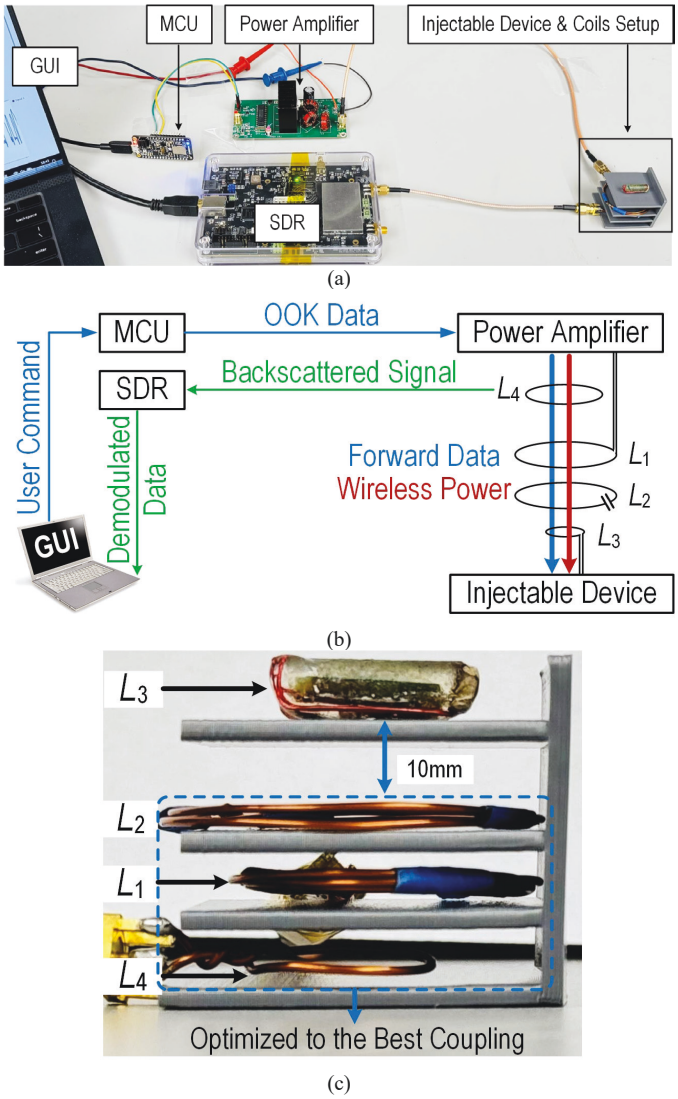

Fig. 15. (a) Setup and (b) schematic of the wireless power and data transmission verification. (c) Detailed configuration of the coils.

the PDL on L_3 within 2-4 mW. As shown in Fig. 16a, the measured PLR remains under 0.2 % when PDL $\leqslant$ 3 mW, which is well enough to power the device at its highest power configuration. This indicates reliable data transmission despite interference from the power carrier. Next, we fixed the PDL to L_3 at 3 mW and manually varied the distance between the L_2 and L_3 to simulate the free movement of the animal subjects. The measured PLR in Fig. 16b remains below 0.2 % when the L_2-L_3 distance is less than 16 mm, but it increases rapidly once the distance exceeds 17 mm. The measured PLR curve indicates reliable wireless data transmission under a stable inductive link and a potentially high data loss rate due to the free movement of the animals. These results suggest that the proposed memory-assisted scheme effectively enhances movement resilience by keeping the PLR below 0.2% by transmitting data only when the inductive link is stable.

B. In Vivo Verification

To evaluate the efficacy of the proposed injectable device, we conducted in vivo experiments on adult Sprague Dawley rats under isoflurane anesthesia. All animal procedures were

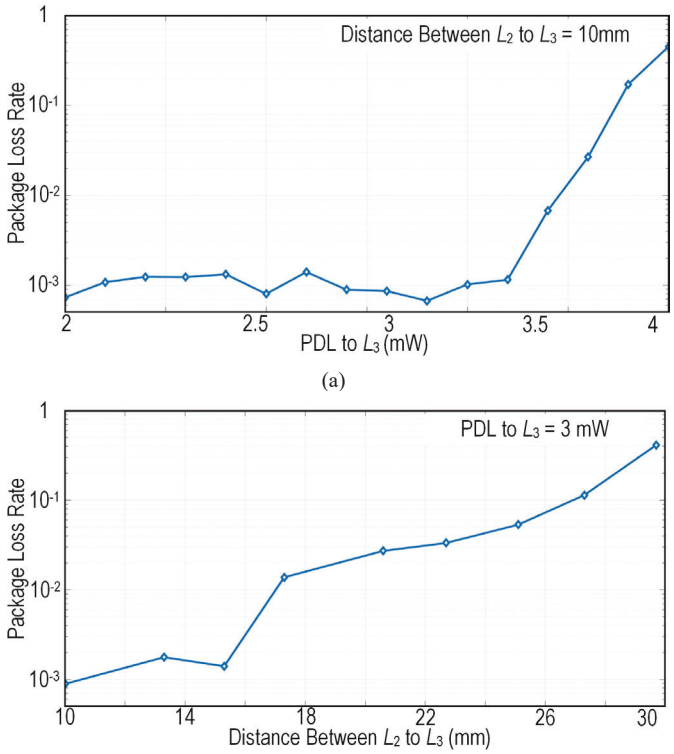

Fig. 16. Measured PLR of the backscatter Tx under (a) varying PDL to L_3 and (b) distances between L_2 to L_3.

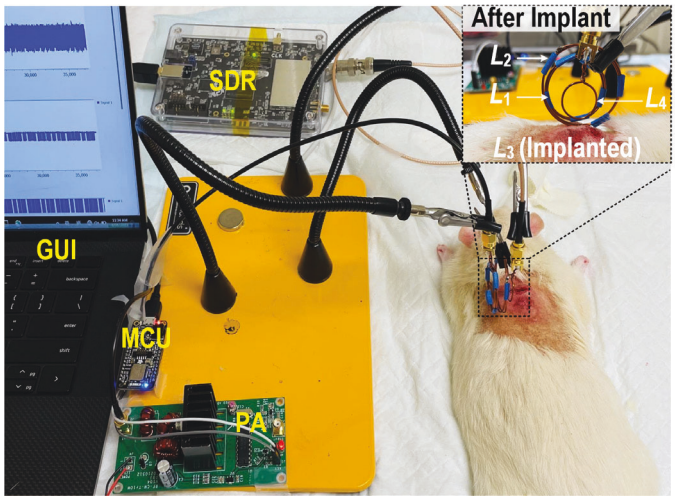

Fig. 17. In vivo experiment setup with an anesthetized rat.

approved by the Institutional Animal Care and Use Committee (IACUC) of NC State University (protocol number: 24-136, Mar 8, 2024; 21-114, May 2, 2021). In Fig. 17, we implanted the proposed injectable device subcutaneously at the thoracic area on the dorsal side of the rat. The PA and MCU generated the OOK-modulated 13.56 MHz carrier to wirelessly transfer user commands and power to the injectable device through the 3-coil inductive link ($L_1 \rightarrow L_2 \rightarrow L_3$). The SDR Rx received and demodulated the backscattered signal through the 4-coil inductive link ($L_3 \rightarrow L_2 \rightarrow L_1 \rightarrow L_4$) before sending it to the GNU Radio and MATLAB GUI running on the PC. Thanks to the tolerance to coil misalignment, the optimized L-shape L_3

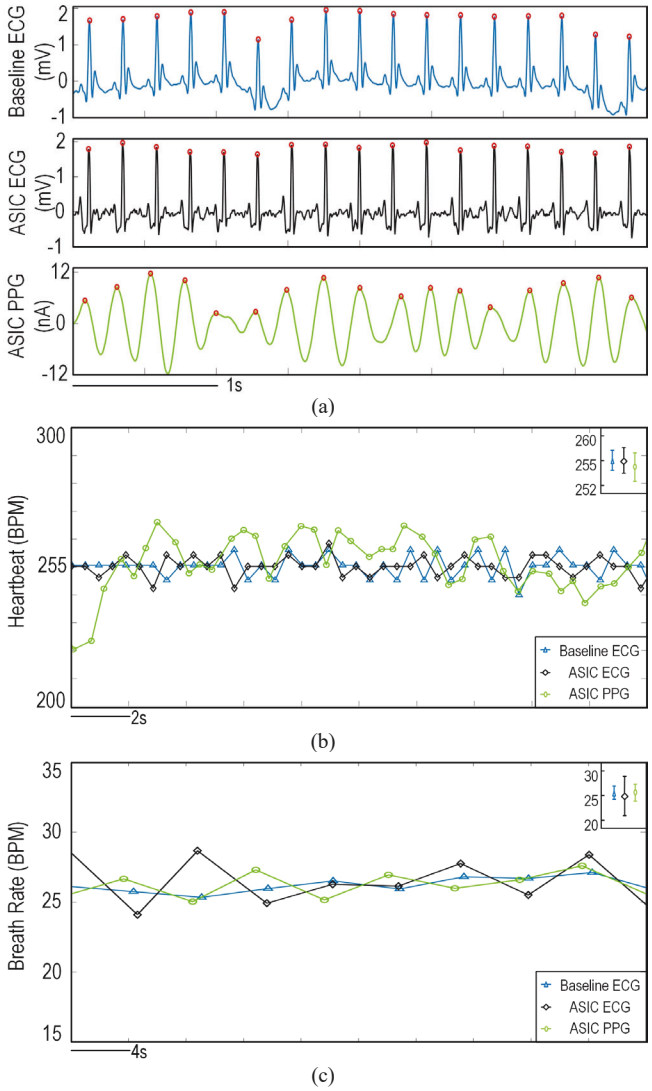

Fig. 18. (a) Measured waveforms of the ASIC-recorded PPG, ASIC-recorded ECG, and baseline ECG in the time domain. (b) Extracted HR and BR from the transient waveforms.

enhances the setup flexibility of the coils. Meanwhile, a reference commercial system (Go Direct™ EKG Sensor, Vernier Software & Technology) recorded the baseline ECG signals simultaneously to verify the accuracy of the physiological signals recorded by the ASIC.

Fig. 18a presents transient waveforms of the ASIC-recorded PPG, baseline ECG, and AISC-recorded ECG. The physiological patterns of the baseline ECG and ASIC-recorded ECG matched with each other, validating the accuracy of the ECG recording and the wireless data and power transmission of the injectable device. To extract the heartbeat (HR) and breath rate (BR), we employed the peak detection algorithm to the recorded transient waveforms. As shown in Fig. 18b, the three transient waveforms indicate an average HR of 255±2 beats per minute (BPM) and an average BR of 25±0.7 BPM. Furthermore, in a separate rat subject, the same experiment and data analysis yielded an average HR of 259±3.3 BPM and an average BR of 27±0.5 BPM. The discrepancies of the extracted HR and BR from the three recorded physiological signals are

below 6 %. The consistent HR and BR results obtained from the two rat subjects validate the reliability of the proposed device.

V. Discussion

While in vivo experiments on anesthetized rats, utilizing WPT and wireless data communication, can effectively demonstrate the functionality of the proposed injectable device and system, we plan to further extend our system implementation to freely moving animals in our future works. This will allow us to further improve the system's reliability by adapting to more realistic and complex conditions on freely moving animals. To accommodate both large and small animals, we will adapt different system configurations. Meanwhile, the selection of the components within the proposed system, such as PA and SDR Rx, should be tailored to each configuration.

In terms of small animals such as rodents, we will employ the EnerCage-HomeCage (EnerCage-HC) system for WPT to the injectable device [37]. The EnerCage-HC, built around the standard rodent homecage, can continuously deliver wireless power to the injectable device through a 13.56 MHz inductive link while the animal freely moves within the cage. The SDR Rx will be located surrounding the EnerCage-HC to receive the backscatter signal from the injectable device. In terms of large animals such as cows, we will develop a battery-powered backpack. Inside the backpack, the PA drives the Tx coil to wirelessly deliver power to the injectable device, while the SDR Rx, with its antenna coupled to the Tx coil, collects backscatter data and transmits it to the end user.

VI. Conclusion

This paper introduces a wireless multimodal physiological monitoring ASIC fabricated in the TSMC standard 180 nm process. The ASIC can be assembled in a miniature cylindrical injectable form factor to monitor subcutaneous body temperature, PPG, and ECG. To achieve a miniature device, we introduce a high Q-factor L-shape Rx coil, ensuring robust coupled and high PTE against coil misalignment while reducing coil and component counts by reusing the Rx coil for both data and power links. To ensure sufficient WPT using such a miniature Rx coil, the ASIC functions alternatively between a regular recording and a power-saving sleep mode, leading to a 2.55 µW ultra-low power consumption. All AFEs are designed for energy efficiency and meet performance requirements for animal physiological monitoring. To facilitate reliable data transmission despite the animal movement, we propose a memory-assisted backscatter Tx, archiving a PLR below 0.2 % under the PDL of 3 mW. In vivo measurements are conducted to confirm the functionality of the proposed injectable device.

References

[1] H. Kim *et al.*, "32.1 A behind-the-ear patch-type mental healthcare integrated interface with 275-fold input impedance boosting and adaptive multimodal compensation capabilities," in *2023 IEEE International Solid-State Circuits Conference (ISSCC)*, 2023: IEEE, pp. 1-3.

[2] Y.-S. Shu *et al.*, "26.1 A 4.5 mm 2 multimodal biosensing SoC for PPG, ECG, BIOZ and GSR acquisition in consumer wearable devices," in *2020 IEEE International Solid-State Circuits Conference-(ISSCC)*, 2020: IEEE, pp. 400-402.

[3] Y. Han *et al.*, "A Wirelessly Powered Scattered Neural Recording Wearable System," *IEEE Transactions on Biomedical Circuits and Systems,* 2024.

[4] T. Seol *et al.*, "33.11 A Hybrid Recording System with 10kHz-BW 630mV PP 84.6 dB-SNDR 173.3 dB-FOM SNDR and 5kHz-BW 114dB-DR for Simultaneous ExG and Biocurrent Acquisition," in *2024 IEEE International Solid-State Circuits Conference (ISSCC)*, 2024, vol. 67: IEEE, pp. 562-564.

[5] R. Agarwala *et al.*, "A 0.6 V 785-nW multimodal sensor interface IC for ozone pollutant sensing and correlated cardiovascular disease monitoring," *IEEE Journal of Solid-State Circuits,* vol. 56, no. 4, pp. 1058-1070, 2021.

[6] J. Lázaro *et al.*, "Wearable armband device for daily life electrocardiogram monitoring," *IEEE Transactions on Biomedical Engineering,* vol. 67, no. 12, pp. 3464-3473, 2020.

[7] S. I. Park *et al.*, "Soft, stretchable, fully implantable miniaturized optoelectronic systems for wireless optogenetics," *Nature biotechnology,* vol. 33, no. 12, pp. 1280-1286, 2015.

[8] A. D. Mickle *et al.*, "A wireless closed-loop system for optogenetic peripheral neuromodulation," *Nature,* vol. 565, no. 7739, pp. 361-365, 2019.

[9] G. Shin *et al.*, "Flexible near-field wireless optoelectronics as subdermal implants for broad applications in optogenetics," *Neuron,* vol. 93, no. 3, pp. 509-521. e3, 2017.

[10] X. Yu *et al.*, "Skin-integrated wireless haptic interfaces for virtual and augmented reality," *Nature,* vol. 575, no. 7783, pp. 473-479, 2019.

[11] D. J. Murphy *et al.*, "Respiratory inductive plethysmography as a method for measuring ventilatory parameters in conscious, non-restrained dogs," *Journal of pharmacological and toxicological methods,* vol. 62, no. 1, pp. 47-53, 2010.

[12] W. Erhardt *et al.*, "The use of pulse oximetry in clinical veterinary anaesthesia," *Journal of the Association of Veterinary Anaesthetists of Great Britain and Ireland,* vol. 17, no. 1, pp. 30-31, 1990.

[13] N. Oliver *et al.*, "HealthGear: a real-time wearable system for monitoring and analyzing physiological signals," in *International Workshop on Wearable and Implantable Body Sensor Networks (BSN'06)*, 2006: IEEE, pp. 4 pp.-64.

[14] D. P. Tobon *et al.*, "Spectro-temporal electrocardiogram analysis for noise-robust heart rate and heart rate variability measurement," *IEEE journal of translational engineering in health and medicine,* vol. 5, pp. 1-11, 2017.

[15] L. C. Wu *et al.*, "In vivo evaluation of wearable head impact sensors," *Annals of biomedical engineering,* vol. 44, pp. 1234-1245, 2016.

[16] L. B. Wood, "Motion artifact reduction for wearable photoplethysmogram sensors using micro accelerometers and Laguerre series adaptive filters," Massachusetts Institute of Technology, 2008.

[17] H. J. Williams *et al.*, "Future trends in measuring physiology in free-living animals," *Philosophical Transactions of the Royal Society B,* vol. 376, no. 1831, p. 20200230, 2021.

[18] S. S. Chowdhury *et al.*, "Robust heart rate estimation from ppg signals with intense motion artifacts using cascade of adaptive filter and recurrent neural network," in *TENCON 2019-2019 IEEE Region 10 Conference (TENCON)*, 2019: IEEE, pp. 1952-1957.

[19] Y. Chen *et al.*, "A wearable physiological detection system to monitor blink from faint motion artifacts by machine learning method," *IEEE Sensors Journal,* 2023.

[20] A. Q. Javaid *et al.*, "Quantifying and reducing motion artifacts in wearable seismocardiogram measurements during walking to assess left ventricular health," *IEEE Transactions on Biomedical Engineering,* vol. 64, no. 6, pp. 1277-1286, 2016.

[21] Z. Yu *et al.*, "33.6 A Millimetric Batteryless Biosensing and Stimulating Implant with Magnetoelectric Power Transfer and 0.9 pJ/b PWM Backscatter," in *2024 IEEE International Solid-State Circuits Conference (ISSCC)*, 2024, vol. 67: IEEE, pp. 551-553.

[22] L. Zhao *et al.*, "33.9 A Miniature Neural Interface Implant with a 95% Charging Efficiency Optical Stimulator and an 81.9 dB SNDR ΔΣM-Based Recording Frontend," in *2024 IEEE International Solid-State Circuits Conference (ISSCC)*, 2024, vol. 67: IEEE, pp. 558-560.

[23] F. Marefat *et al.*, "26.7 A 280µW 108dB DR readout IC with wireless capacitive powering using a dual-output regulating rectifier for implantable PPG recording," in *2020 IEEE International Solid-State Circuits Conference-(ISSCC)*, 2020: IEEE, pp. 412-414.

[24] V. W. Leung *et al.*, "Distributed microscale brain implants with wireless power transfer and Mbps bi-directional networked communications," in *2019 IEEE Custom Integrated Circuits Conference (CICC)*, 2019: IEEE, pp. 1-4.

[25] T. Yousefi *et al.*, "An implantable optogenetic neuro-stimulator SoC with extended optical pulse-width enabled by supply-variation-immune cycled light-toggling stimulation," *IEEE Transactions on Biomedical Circuits and Systems,* vol. 16, no. 4, pp. 557-569, 2022.

[26] P. Ahmmed *et al.*, "A Subcutaneously Injectable Implant for Multimodal Physiological Monitoring in Animals," *IEEE Sensors Journal,* 2024.

[27] E. Y. Chow *et al.*, "A miniature-implantable RF-wireless active glaucoma intraocular pressure monitor," *IEEE Transactions on Biomedical Circuits and Systems,* vol. 4, no. 6, pp. 340-349, 2010.

[28] I. E. Araci *et al.*, "An implantable microfluidic device for self-monitoring of intraocular pressure," *Nature medicine,* vol. 20, no. 9, pp. 1074-1078, 2014.

[29] R. Feiner *et al.*, "Tissue–electronics interfaces: from implantable devices to engineered tissues," *Nature Reviews Materials,* vol. 3, no. 1, pp. 1-16, 2017.

[30] H. Guo *et al.*, "Wireless implantable optical probe for continuous monitoring of oxygen saturation in flaps and organ grafts," *Nature communications,* vol. 13, no. 1, p. 3009, 2022.

[31] J. Lee *et al.*, "Neural recording and stimulation using wireless networks of microimplants," *Nature Electronics,* vol. 4, no. 8, pp. 604-614, 2021.

[32] L. Zhao *et al.*, "A Wireless Multimodal Physiological Monitoring ASIC for Animal Health Monitoring Injectable Devices," *IEEE Transactions on Biomedical Circuits and Systems,* 2024.

[33] D. Lovely *et al.*, "Epoxy moulding system for the encapsulation of microelectronic devices suitable for implantation," *Medical and Biological Engineering and Computing,* vol. 24, pp. 206-208, 1986.

[34] Y. Jia *et al.*, "A trimodal wireless implantable neural interface system-on-chip," *IEEE transactions on biomedical circuits and systems,* vol. 14, no. 6, pp. 1207-1217, 2020.

[35] A. Vaz *et al.*, "Full passive UHF tag with a temperature sensor suitable for human body temperature monitoring," *IEEE Transactions on Circuits and Systems II: Express Briefs,* vol. 57, no. 2, pp. 95-99, 2010.

[36] D. Bharadia *et al.*, "Full duplex radios," in *Proceedings of the ACM SIGCOMM 2013 conference on SIGCOMM*, 2013, pp. 375-386.

[37] Y. Jia *et al.*, "Position and orientation insensitive wireless power transmission for EnerCage-Homecage system," *IEEE Transactions on Biomedical Engineering,* vol. 64, no. 10, pp. 2439-2449, 2017.